Near-wall characteristics of non-equilibrium turbulent boundary layers on rough walls

Junlin Yuan[1]†, Matthew Gatzek[1] and Saurabh Pargal[1]

[1]Michigan State University, Michigan, USA

(Received xx; revised xx; accepted xx)

Engineering models of rough-wall turbulent flows rely on reduced model of the near-wall layer of flow modified by roughness (i.e. the roughness sublayer) to provide boundary conditions to the flow above. Understanding sublayer response to pressure gradients and the pressure gradient history is crucial for developing physics-based turbulence closures. This work examines characteristics of the roughness sublayer using roughness-resolved simulation data of two flat-plate boundary layers: one direct numerical simulation with strong non-equilibrium favorable pressure gradients (Yuan and Piomelli, *J. Fluid Mech.* **780**:192-214, 2015) and a large-eddy simulation with a suction-blowing freestream that induces both adverse and favorable pressure gradients. The sublayer thickness y_R is found to be constant in attached-flow regions, regardless of pressure gradients. When using a set of sublayer scales (U_R, y_R) for normalization (where U_R is the local streamwise mean velocity at the elevation y_R), an overall self-similarity is observed for the total drag, mean velocity, and dispersive stresses inside the sublayer, suggesting that the time-mean flow is in quasi-equilibrium despite varying pressure gradients. For the Reynolds stress profiles, self-similarity under the present normalization is not present in general, but the Reynolds stress anisotropy appears to satisfy the weak-equilibrium condition. The observed invariance properties of the roughness sublayer flow indicate potential for extending existing sublayer-unresolved turbulence models to rough-wall non-equilibrium flows and provide a way to assess existing roughness treatments in turbulence models.

Key words:

1. Introduction

Surface roughness is present across a wide range of applications. In predictive engineering models of turbulent flows, such as Reynolds-averaged Navier-Stokes (RANS) models and wall-modeled large-eddy simulations (WMLES), roughness is usually not resolved, but instead its gross effects on the mean velocity and stresses are modeled. In such approaches, the roughness sublayer (RSL)—the layer where the mean flow is dynamically affected by roughness—is ignored. Instead, often the hydrodynamic drag of roughness (an integral of the total drag generated inside the RSL) and turbulence properties (turbulence scales and Reynolds stresses, etc.) at the edge of the sublayer are used as boundary conditions of the layer above.

Since most surfaces are neither flat nor perfectly aligned with the freestream, pressure gradients are usually present in real flows and are often non-equilibrium. Here, the

† Email address for correspondence: junlin@msu.edu

definition used by Klewicki *et al.* (2024) for equilibrium flows is adopted: these are self-preserving flows where the various statistical profiles admit an invariant representation under normalizations that properly employ locally defined characteristic scales. Volino *et al.* (2022, 2024) and Klewicki *et al.* (2024) provided recent reviews on experimental and numerical observations, analytical development, and modeling efforts on non-equilibrium turbulent boundary layers on smooth or rough walls. Main features of non-equilibrium flows include departure of the mean velocity profile from the equilibrium state (e.g. the canonical logarithmic mean velocity) and the effects of both the pressure gradient and its history on turbulence fluctuations. With the distance from the wall scaling shown to still hold in pressure gradient flows (Romero *et al.* 2022*a*), the departure from the logarithmic profile may be due to the change in the velocity scale across the boundary layer (Romero *et al.* 2023). Roughness tends to promote faster turbulence response compared to that on a smooth wall in an FPG (favorable pressure gradient) flow. Outer layer similarity appears to hold in pressure gradient flows under some conditions including FPG flows or APG (adverse pressure gradient) flows with matching history (Volino & Schultz 2023). The same study showed that the sandgrain roughness height k_s (determined from local logarithmic mean velocity profiles) appears invariant with pressure gradients.

Non-equilibrium boundary layers over rough walls have been modeled using RANS (e.g., Yuan *et al.* 2014; Dutta *et al.* 2016). While RANS simulations successfully captured the overall flow evolution, they struggle with accurately reproducing non-equilibrium flow behaviors. For example, in a flat-plate FPG flows the hydrodynamic drag was significantly under-predicted by RANS Volino *et al.* (2024). In a flat-plate suction-blowing boundary layer that involves separation, RANS did not accurately capture the wall friction near the separation point as the roughness sublayer, in which the flow reversal occurs ahead of the location of streamline separation, is not resolved in the model (Dutta *et al.* 2016). In addition, different roughness treatments lead to significantly different predictions of the flow with the same k_s (Volino *et al.* 2024; Yuan *et al.* 2014). Existing roughness treatments prescribe $U(y)$ or turbulence quantities at the rough-wall boundary (either by directly setting the value or by indirectly shifting wall-normal statistical profiles by an offset) as functions of k_s, treated as a constitutive property of that surface. Examples include the k_s-based RANS model modifications of Wilcox (2006) and Aupoix & Spalart (2003), the discrete element method (e.g. Taylor *et al.* 1985), and the composite sublayer $U(y)$ profile model of Brereton *et al.* (2021). When applied in non-equilibrium flows, these treatments effectively assume that the modeled roughness effect maintains the equilibrium condition locally. The global effect of the unresolved RSL on the outer-layer velocity and stresses are assumed to stay unchanged as in an equilibrium flow. Despite recent focus on rough-wall non-equilibrium boundary layers (e.g. Volino & Schultz 2023; Vishwanathan *et al.* 2023), the major focus is not on obtaining well-resolved statistics in the RSL. It is unclear how the sublayer flow, characterized by its thickness, drag generation and velocity statistics, depends on the streamwise pressure gradient and its history.

Most past studies resolving the RSL focused on equilibrium wall-bounded flows, such as flat-plate boundary layers under zero-pressure gradients (ZPG) or fully-developed channel flows. Mangavelli & Yuan (2023) and Mangavelli *et al.* (2021) analyzed direct numerical simulations (DNS) of transient half-channel flows on rough walls, as they undergo non-equilibrium response to a step acceleration of the bulk velocity. Notably, they observed that the friction velocity $u_\tau(t)$ scales with the mean velocity at the edge of the RSL, $U_R(t)$, and not on the bulk velocity. In addition, the wake kinetic energy (WKE) accelerates at the pace of $U_R^2(x)$, while the turbulence kinetic energy (TKE) lags behind. These findings are similar to the observations of Yuan & Piomelli (2015) on a

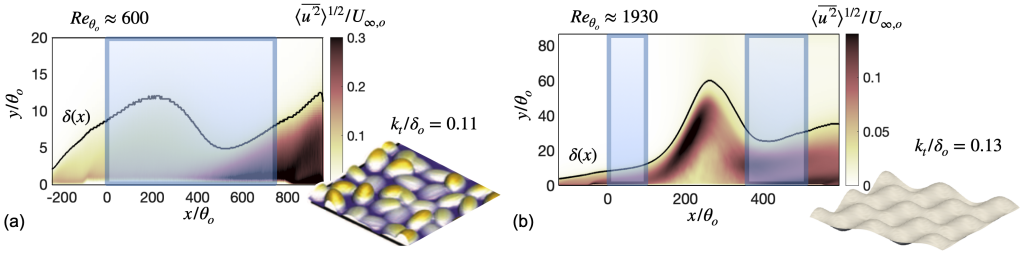

FIGURE 1. Boundary layer development: (a) FPG case and (b) suction-blowing case. Contour shows u' intensity. Boxes mark attached-flow regions examined in this work.

spatially developing flat-plate boundary layer under non-equilibrium FPGs on a rough wall. The results indicated that the drag coefficient of the roughness may be invariant in non-equilibrium accelerated flow when normalized appropriately, which is potentially useful in rough-wall turbulence modeling. In addition, although a small number of studies were carried out focusing on the RSL in non-equilibrium accelerating flow, few studies are available on decelerating ones.

The objective of this work is to characterize the RSL flow in non-equilibrium FPG and APG boundary layers. This study focuses on extracting self-similar or invariant properties of statistical flow quantities inside the RSL. Simulation data include an existing DNS of an FPG flow (i.e. the FPG case, Yuan & Piomelli 2015) and the data of a new LES simulation of separating boundary layer under a suction then blowing freestream (the "suction-blowing" case). The latter is subjected to strong APGs that lead to boundary layer separation, followed by an FPG region to force reattachment. The analyses focus on the attached flow regions.

2. Problem formulation

This study utilizes data from two different simulations of rough-wall boundary layers: an existing DNS of an FPG flow (Yuan & Piomelli 2015) and a new LES of a suction-blowing boundary layer conducted for this study. Figure 1 shows the evolution of the boundary layer in both cases based on the intensity of the streamwise Reynolds stress (with the notations introduced in this section below). In the suction-blowing case, a separation bubble is formed.

For both simulations, the incompressible flow of a Newtonian fluid is governed by the equations of conservation of mass and momentum:

$$\frac{\partial u_i}{\partial x_i} = 0, \tag{2.1}$$

$$\frac{\partial u_j}{\partial t} + \frac{\partial u_i u_j}{\partial x_i} = -\frac{\partial P}{\partial x_j} - \frac{\partial \tau_{ij}}{\partial x_i} + \nu \nabla^2 u_j + f_j^{IB}, \tag{2.2}$$

where x_1, x_2 and x_3 (or x, y and z) are, respectively, the streamwise, wall-normal and spanwise directions, and u_j (or u, v and w) are the filtered velocity components in those directions; $P = p/\rho$ is the modified pressure, ρ the density and ν the kinematic viscosity. The term f_j^{IB} in Equation 2.2 is a body force of the immersed boundary method (Yuan & Piomelli 2014*b*) used to impose non-slip, non-penetration boundary conditions at the roughness surface. For our LES simulation (suction-blowing case), the sub-filter stress τ_{ij} is modeled using a dynamic eddy-viscosity model (Germano *et al.* 1991) based on the Lagrangian-averaging procedure, while for the DNS data (FPG

Cases	Flow parameters	Grid points	Resolution	Domain
FPG (DNS)	$Re_\theta = 612$–1787, $k_t/\delta = 0.05$–0.11, $k_t^+ = 34$–119.	$(n_i, n_j, n_k) =$ (4608, 270, 512), $(N_i, N_k) = (5\text{–}8, 10)$.	$\Delta x^+ = 10$–21, $\Delta y^+_{min} = 0.2$–0.7, $\Delta z^+ = 5$–14.	$(L_x, L_y, L_z)/\theta_o =$ (1203, 54, 54)
Suction-blowing (LES)	$Re_\theta = 1924$–8315, $k_t/\delta_o = 0.13$, $k^+_{t,o} = 132$.	$(n_i, n_j, n_k) =$ (2560, 704, 384), $(N_i, N_k) = (13, 19)$.	$\Delta x^+ = 20$–35, $\Delta y^+_{min} = 0.3$–0.6, $\Delta z^+ = 15$–24.	$(L_x, L_y, L_z)/\theta_o =$ (720, 86, 75)

TABLE 1. Simulation parameters for the existing FPG case (Yuan & Piomelli 2015) and the new suction-blowing case. n_i, n_j and n_k are the total numbers of grid points in x, y and z; (N_i, N_k) are the numbers of grid points per roughness element in x and z directions; Δx^+, Δy^+_{min} and Δz^+ are the grid spacings in wall units, in x, y (minimal value) and z; (L_x, L_y, L_z) are the domain dimensions.

case) this term is zero. The governing equations are solved on a staggered grid using second-order central differences for all terms and second-order Adams-Bashforth semi-implicit time advancement. Double averaging is performed; $\overline{(\cdot)}$ and $\langle\cdot\rangle$ represent time averaging and intrinsic plane averaging, respectively. $\widetilde{(\cdot)}$ and $(\cdot)'$ represent form-induced and turbulent fluctuations.

For both cases, the inlet turbulence is generated by the recycling and rescaling method (Lund *et al.* 1998) in the region upstream of $x/\theta_o = 0$; a convective boundary condition (Orlanski 1976) is used at the exit. Periodic boundary conditions are applied at the spanwise (z) direction. The reference location (i.e. the location where x is zero) is taken as the location where the rough-wall ZPG flow is fully developed; this reference location is the start of the useful region. The momentum thickness (θ) and boundary layer edge velocity (U_e) at the reference location (i.e. θ_o and $U_{e,o}$, respectively, where the subscript o represents the value at the reference location) are used as the reference length and velocity scales. The two x boundary conditions are imposed on a smooth-wall flow. To prevent a long distance of flow adjustment from an abrupt smooth-to-rough transition, the size of roughness elements is varied gradually (while keeping the same aspect ratio) during the transition before and after the useful region with roughness, in a way similar to Wu & Piomelli (2018). It is verified that a fully developed rough-wall flow is achieved at $x/\theta_o = 0$. Table 1 lists the set-up parameters of both cases. The two cases are discussed in detail as follows.

The FPG case is a DNS simulation with $Re_\theta = \theta U_e/\nu$ from around 600 to 850 from Yuan & Piomelli (2015). At the reference location ($x/\theta_o = 0$), $Re_\theta = 612$ and $Re_\tau = \delta u_\tau/\nu = 311$ (where δ is the boundary layer thickness, calculated based on a threshold of the local ratio $\langle\overline{u'^2}\rangle^{1/2}/U = 0.03$ and is shown in Figure 1(a)). A sandgrain roughness consisting of densely distributed, randomly rotated ellipsoids (Yuan & Piomelli 2014*b*) is imposed on the wall (see Figure 1(a)), with the roughness peak-to-trough height k_t up to 0.11δ. An almost three-fold acceleration of streamwise freestream velocity $U_\infty(x)$ is imposed at the top boundary from $x/\theta_o = 0$ to the end of the useful domain at $x/\theta_o \approx 750$. More details of the simulation are available from Yuan & Piomelli (2015).

The set-up of the suction-blowing boundary layer is similar to that of Wu & Piomelli (2018). A suction-blowing distribution of wall-normal velocity $V_\infty(x)$ is imposed on the top boundary to generate APG and downstream FPG regions in the boundary

layer. At the reference location, $Re_\theta = 1924$ and $Re_\tau = 1034$. The resolution Δx_i^+ is comparable to existing LES studies of rough-wall flows (Wu & Piomelli 2018; Yuan & Piomelli 2014*a*). Here, superscript + indicates normalization in wall units ($u_\tau = \sqrt{\tau_w/\rho}$ and ν/u_τ, where τ_w is the wall shear stress). The domain size is comparable to that of Wu & Piomelli (2018) which imposed a similar mean pressure gradient profile. On the bottom wall, a roughness different from the random sandgrains of Wu & Piomelli (2018) is used. A three-dimensional harmonic roughness (see Figure 1(b)) is imposed as $h(x,z) = (k_t/2)\cos[(2\pi/\lambda)x]\cos[(2\pi/\lambda)z] + k_t/2$, where h is the local elevation of rough surface measured from the roughness trough, which is taken as $y = 0$. The roughness wavelength is given by $\lambda = k_t/0.28$. The roughness geometry corresponds to Case 60_424 of Chan *et al.* (2015). The use of a regular roughness allows performing local phase averaging to study the detailed flow pattern inside the RSL methodologically. Such analysis is not presented here. However, this choice of roughness geometry does not affect the current RSL characterization. The roughness height $k_t/\delta = 0.13$ at $x/\theta_o = 0$ and decreases along x, to around 0.04 in the reattached boundary layer. The useful flow domain is between $x/\theta_o = 0$ and 500.

The discussion of results is focused on the attached flow regions highlighted in Figure 1: $x/\theta_o \in [0, 90]$ and $x/\theta_o \in [360, 500]$ for the suction-blowing flow and $x/\theta_o \in [0, 750]$ for the FPG flow. The x/θ_o bounds are selected where boundary effects from roughness transitions at inlet and outlet are negligible. Despite different geometries and pressure gradient histories, both cases provide suitable data for RSL behavior in non-equilibrium flows due to their strong bidirectional pressure gradients. However, due to these differences between the case set-up, the focus of results discussion will be on comparing trends, instead of values, between the two cases. To provide further quantitative insights to the effect of pressure gradients, future work would need to focus on flows with the same roughness geometry and systematically prescribed pressure gradient history (or equilibrium flows). This work is a first step toward this goal, by focusing on invariant properties of the RSL in two drastically different pressure-gradient flows.

3. Results

3.1. *Boundary layer development*

The strengths of pressure gradients of the two cases in the attached flow regions are quantified using parameters $K_e = (\nu/U_e^2)U_e'$ and $\beta_e = (\delta^*/\tau_w)P_e' = -Re_{\delta^*}(U_e/u_\tau)^2 K_e$, where $\tau_w(x) = \int \overline{f_1^{IB}}(x,y,z)dydz/(L_y L_z)$, δ^* is the displacement thickness and P_e is the dynamic pressure at the edge of the boundary layer. These parameters have distinct physical interpretations: K_e represents the relative influence of viscous effects compared to inertial effects under a pressure gradient, while β_e captures the relative importance of pressure forces to wall shear stress. Figures 2(a,b) show that strong pressure gradients are reached in both cases. For the APG flow, the boundary layer separation indicates strong non-equilibrium APG. For the FPG flow, K_e values reach approximately 3.5×10^{-6}, comparable to values (2.5×10^{-6} to 3.5×10^{-6}) reported in previous studies of strong FPG flows (Volino *et al.* 2024), where reverse transition toward a quasi-laminar state can occur in the case of a smooth-wall flow (Spalart 1986; Piomelli & Yuan 2013). The β_e values in FPG flows are typically smaller in magnitude (typically up to around -0.5 and sometimes -1 in literature) (Volino *et al.* 2024) due to the increased friction velocity and reduced boundary layer thickness under FPG. In both cases, the non-constant values of β_e indicate that the boundary layers are non-equilibrium.

The variation of friction coefficient based on the edge velocity $C_{f,e} = |\tau_w|/(1/2\rho U_e^2)$

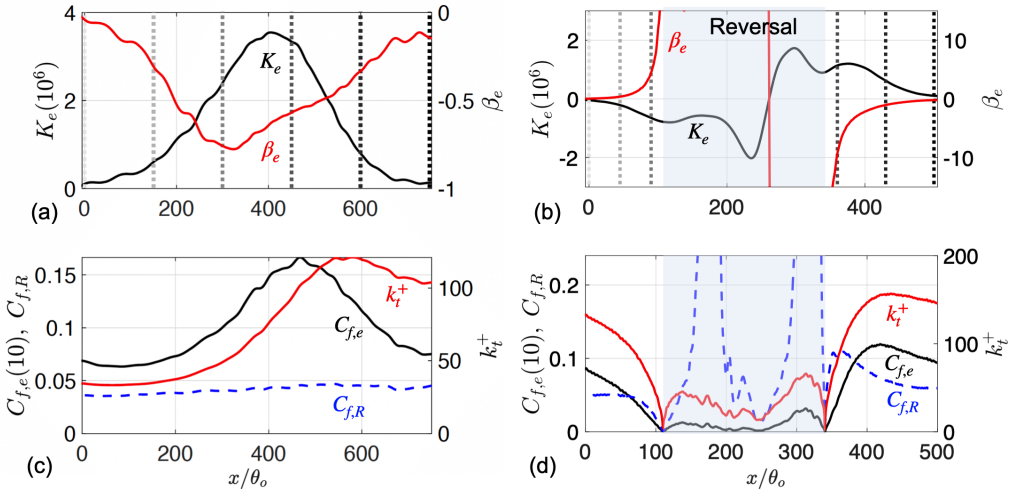

FIGURE 2. Boundary layer development in the FPG (a,c) and suction-blowing (b,d) cases. In (a,b), vertical dotted lines mark locations for statistics profiles discussed in Section 3. In (b,d), shaded areas indicate the zone of flow reversal.

shows a faster drag increase on the rough wall in the FPG flow than the increase of freestream velocity (Figure 2(c)). In the suction-blowing flow (Figure 2(d)), $C_{f,e}$ decreases with x inside the APG zone till the region of flow reversal for $x/\theta_o \in (110, 330)$ with $\tau_w < 0$. At $x/\theta_o \approx 330$, the flow reattaches to the wall at the second location where $C_{f,e} = 0$.

The variation of the roughness Reynolds number based on the peak-to-trough height $k_t^+ = k_t u_\tau/\nu$ shown in Figure 2 (c,d) provides information regarding the roughness regime. For the sandgrain roughness used in the FPG flow, Yuan & Piomelli (2015) showed that flows with this roughness geometry reach the fully rough regime at $k_t^+ \approx 90$ in channel flows. The present k_t^+ values (Figure 2(c)) show that the flow is transitionally rough at $x/\theta_o = 0$ and becomes nominally fully rough at $x/\theta_o \approx 450$. For the harmonic roughness in the suction-blowing case, considering that this roughness geometry has a threshold of fully rough regime at $k_t^+ \approx 50$ in channel flows (Chan *et al.* 2015), Figure 2(d) shows that the flow is fully rough at $x/\theta_o = 0$. As k_t^+ decreases along x due to a decrease of u_τ approaching the separation point, the flow becomes nominally transitionally rough at $x/\theta_o \approx 100$.

Figures 2(c,d) also show the friction coefficient normalized by the roughness sublayer edge velocity, $C_{f,R} = \tau_w/(1/2\rho U_R^2)$, where U_R is the mean velocity at the edge of the roughness sublayer (to be defined in Section 3.2). In contrast to the $C_{f,e}$ variation, $C_{f,R}$ remains nearly constant in attached flow regions at large roughness Reynolds numbers for both cases, suggesting that τ_w scales with U_R^2 rather than U_e^2. The implications of this scaling relationship will be examined in detail in Section 3.3.

3.2. *Characteristic scales of the roughness sublayer*

The RSL, i.e. the layer bounded by the roughness trough elevation and an upper limit at y_R, is defined as the layer in which the time-mean flow displays spatial heterogeneities due to the presence of roughness (Pokrajac *et al.* 2007): $\langle\widetilde{u}^2\rangle^{1/2}/\langle\overline{u}\rangle \geqslant \gamma$, where threshold γ is a small value, taken as 0.1 here. Figure 3 plots the wall-normal profiles of $\langle\widetilde{u}^2\rangle^{1/2}/\langle\overline{u}\rangle$ at various x locations (with darker line color indicating increasing x) for both cases. Logarithmic vertical scaling is used as $U(y)$ zero-crossings resulted from organized

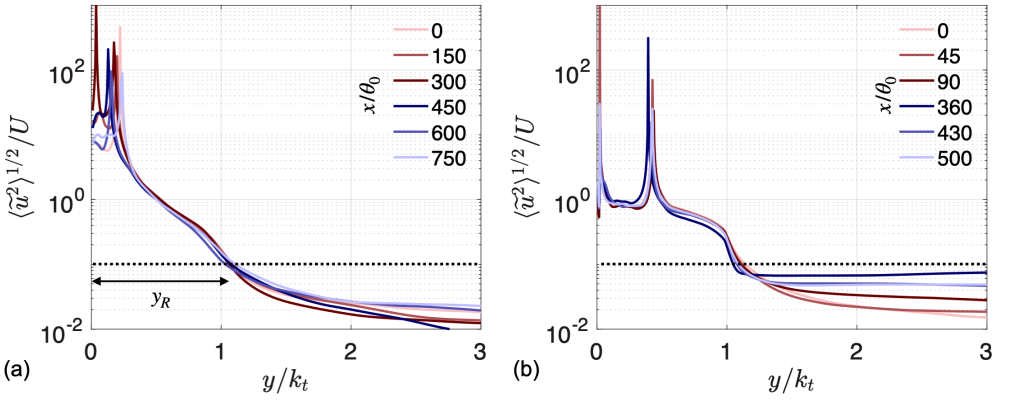

FIGURE 3. Determination of roughness sublayer thickness (y_R, above which $\langle\widetilde{u}^2\rangle^{1/2}/U < 0.1$): (a) FPG case and (b) suction-blowing case.

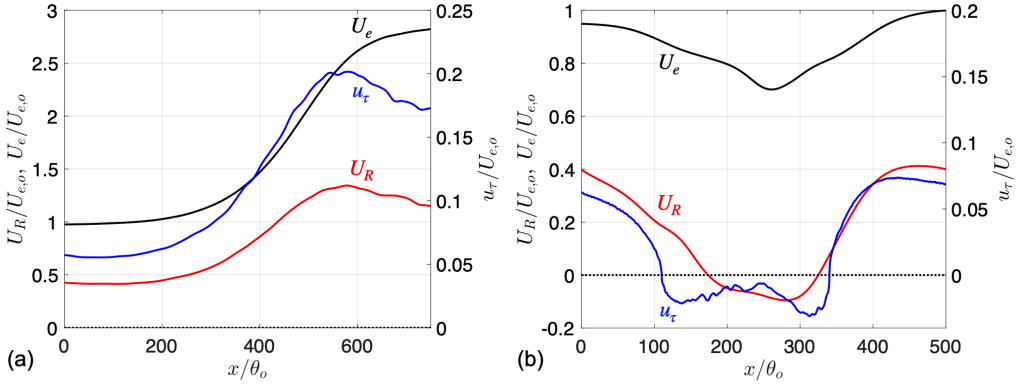

FIGURE 4. Streamwise developments of various velocity scales: outer scale (U_e), inner scale (u_τ) and roughness sublayer scale (U_R): (a) FPG case and (b) suction-blowing case.

recirculation regions (to be shown in Figure 6(b)) yield infinite ratios. The specific profile shapes inside the RSL are not the same between the two cases, since the roughness geometries are different. It was checked that various γ values from 0.15 to 0.3 do not lead to a significant change in the calculated thickness. Results show that $y_R \approx k_t$ and that y_R varies only weakly with x (indicating a weak dependence on pressure gradient), even for the nominally transitionally rough regions: $x/\theta_o = 0$ for FPG flow and $x/\theta_o = 90$ near the separation point for the suction-blowing flow. In the study of temporally accelerating flows by Mangavelli *et al.* (2021), the RSL thicknesses calculated in a similar way were also shown to be independent of time, for different roughness geometries. Therefore, the invariant RSL extent in non-equilibrium boundary layers appears to be robust.

Based on y_R, a RSL velocity scale is defined by $U_R(x) \equiv \langle\overline{u}\rangle(x, y_R)$, representing the RSL edge velocity.

Here for practicality $U_R(x)$ is calculated as $U(x, y_{R,o})$, where $y_{R,o}$ is the RSL thickness at the reference x location. The choice of using a fixed y location to evaluate U_R arises from the observation that y_R is constant in the attached flow region (as shown in Figure 3). Using the local $y_R(x)$ to evaluate U_R instead would face challenges in the detachment region where the dispersive stress profile departs significantly from those shown in Figure 3(b), making it difficult to quantify $y_R(x)$ there.

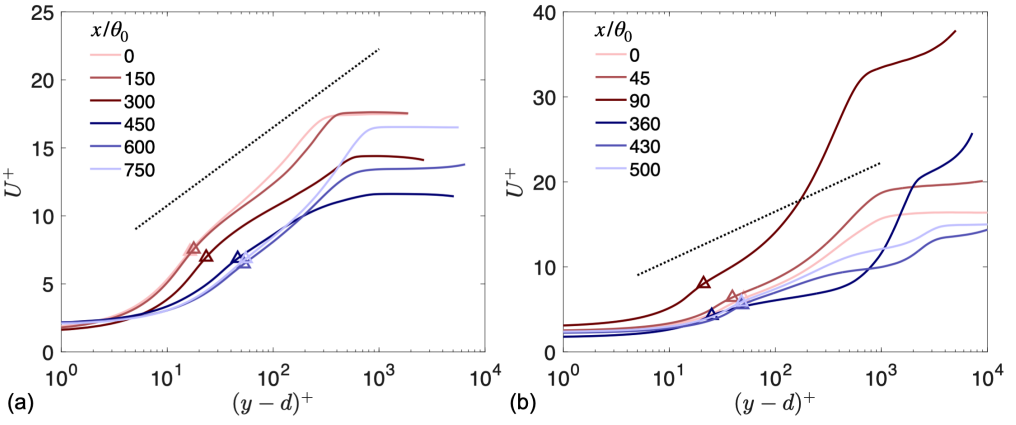

FIGURE 5. Streamwise mean velocity profiles in viscous units: (a) FPG case and (b) suction-blowing case. --- $U^+ = (1/\kappa)\log(y-d)^+ + B$ with $\kappa = 0.4$ and $B = 5.0$.

Figure 4(a) shows the streamwise development of this RSL velocity scale U_R, together with the boundary layer edge velocity U_e and the friction velocity u_τ. In the FPG boundary layer, the relative increase of U_R is greater than that of U_e during flow acceleration: U_R increases by approximately a factor of 2.4 while U_e increases by a factor of about 1.7 in the region $x/\theta_o \in [0, 450]$ In the APG region of the suction-blowing case U_R decreases by a larger percentage than U_e in the region $x/\theta_o \in [0, 150]$. These are signatures of the non-equilibrium boundary layers. In the detachment region shown in Figure 4(b), U_R is negative, indicating reverse flow at the roughness crest. Examining Figure 4(b), one observes different evolutions for u_τ and U_R along the streamwise direction in the suction-blowing case. An important observation is that U_R crosses zero at a location further downstream (at $x/\theta_o \approx 170$) compared to where u_τ becomes zero (at $x/\theta_o \approx 110$). Wu & Piomelli (2018) compared various identification criteria of the separation points on a rough wall and found that the point based on $u_\tau = 0$ occurs significantly more upstream from the actual point of streamline separation. Same observation is found here, with the x location of $U_R = 0$ (a criterion based on the flow above RSL) representing the location where streamline separation occurs. In addition, the asynchronous variations of U_R and U_e suggests that U_R may be a better velocity scale for the flow near the rough wall. Section 3.3 will show that the mean streamwise velocity and wake kinetic energy profiles are invariant in x when normalized using U_R.

3.3. *Time-mean statistics normalized by RSL scales*

In transient accelerated channel flows (Mangavelli *et al.* 2021), $\tau_w(t)$ was found to scale approximately on $U_R(t)^2$. Figures 2(c,d) compare the streamwise evolutions of the drag coefficients obtained based on U_R or U_e for both cases, together with the variation of k_t^+. The scaling of τ_w on U_R^2 is shown to be also the case in the present spatially developing boundary layers in the regions with high k_t^+. $C_{f,R}$ takes an almost constant value in the attached flow regions in both cases, when sufficiently far from the reversal zone with $\tau_w(x) < 0$. This observation suggests that, when $y_R^+ \gg 1$, the drag coefficient (when defined appropriately) is invariant with the imposed streamwise pressure gradient and its history. On the other hand, τ_w does not scale with U_e^2 in either case, as shown by the significantly varying $C_{f,e}$ in Figures 2(c,d). As another note, the infinite $C_{f,R}$ values in Figure 2(d) at $x/\theta_o \approx 170$ and 320 are due to U_R crossing zero at these locations.

Figure 5 shows the double-averaged streamwise velocity profiles in viscous scaling in

the two cases. Here, the y axis is offset by the amount of virtual origin d—defined as the distance from the trough elevation ($y = 0$) to the centroid of the y-profile of the total drag distribution $\langle \overline{f_1^{IB}} \rangle_o(y)$ (Jackson 1981) to collapse the log-law layer. Here, $\langle \cdot \rangle_o = \int (\cdot) dz/Lz$. Yuan & Piomelli (2015) discussed the U^+ profile variation under strong FPG on the rough wall, characterized by an augmentation of the U^+ offset in the logarithmic layer and a milder log-law slope similar to a smooth-wall boundary layer under FPG. The higher offset is consistent with the increase of τ_w. On the other hand, in the suction-blowing boundary layer a strong wake is observed as a result of the APG when x moves toward the separation point, together with a decrease in the logarithmic offset due to the decrease in τ_w. After reattachment ($x/\theta_o \approx 320$), the augmented wake reduces along x toward the equilibrium state. These observations are consistent with those from Wu & Piomelli (2018) for a sandgrain roughness. In addition, the scaling of hydrodynamic drag on U_R^2 as observed above indicates that U_R, when evaluated in plus units, stays approximately constant in attached flows, as $U^+(y_R) \sim 1/\sqrt{C_{f,R}}$, where $C_{f,R}$ is approximately a constant (Figure 2(c)). The y_R locations of the U profiles are marked by triangles in Figure 5. For the FPG case, indeed an almost constant $U^+(y_R)$ value is shown for all x locations. For the suction-blowing case, some variation is observed just before the separation and just after the reattachment (as shown by the profiles at $x/\theta_o = 90$ and 360), consistent with the variation of $C_{f,R}(x)$ in these regions as shown in Figure 2(d).

The scalings of the RSL statistics including mean velocities, Reynolds stresses and dispersive stresses are analyzed next. First, $U(y)$ is plotted using the outer scalings (local values of U_e and δ) in Figure 6(a,b) for the two cases in the attached-flow x locations. The profiles at different x do not collapse in any part of the boundary layer. The near-wall region (i.e. $y/\delta < 0.1$) is characterized by reduction of momentum due to the increased hydrodynamic drag as a result of the roughness. Figure 6(a) shows that acceleration leads to a fuller profile with stronger shear near the wall, explaining the faster increase of U_R than that of U_e (shown in Figure 4(a)), while the opposite is shown in the APG flow in Figure 6(b).

When U_R and y_R are used as scaling variables to non-dimensionalize U and y in Figure 6(c,d), a near-wall collapse is found. Due to the normalization, all profiles pass through points $(0, 0)$ and $(1, 1)$ in these plots. This allows a better collapse of data in the RSL (i.e. region of $y/y_R \in [0, 1]$). Surprisingly, the velocity profile shape in the RSL is shown to vary only weakly with the strongly non-equilibrium boundary layers, even in the regions near the reversal region ($x/\theta_o = 90$ and 360 in Figure 6(d)). A slight change of the profile shape inside the RSL is observed in the FPG flow (Figure 6(c)), which may be explained by a transition from the nominally transitionally rough to the fully rough state. It is unclear why this weak dependency is not observed for the harmonic roughness; a roughness-geometry effect may be present and future work should investigate FPG flow with the same roughness geometry. Near $y = 0$, a layer with negative U values is shown in the case with regular harmonic roughness (Figure 6(d)), while this layer is not present for the random sandgrain roughness (Figure 6(c)). This layer results from organized recirculation regions formed downstream of the harmonic roughness protuberances. The crossings of U past zero leads to the peaks of $\langle \widetilde{u}^2 \rangle^{1/2} / \langle \overline{u} \rangle$ shown in Figure 3. The self-similarity of $U(y)$ inside the RSL when normalized using the RSL scales is a significant finding, as it suggests that models of the RSL $U(y)$ developed using equilibrium-flow data (e.g. the composite profile model of Brereton *et al.* (2021)) may be directly extendible to non-equilibrium boundary layers.

To examine the overall development of the dispersive stresses, y-profiles of the WKE

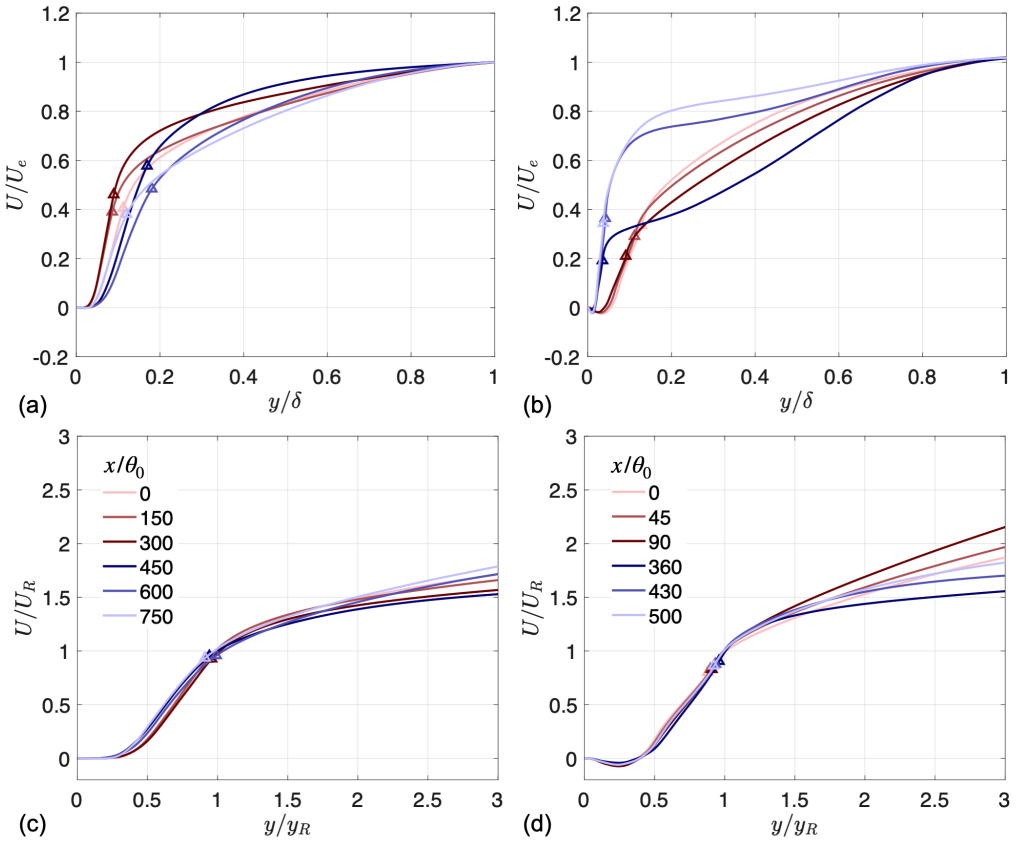

FIGURE 6. (a,b) $U(x, y)$ profiles normalized by local U_e and δ. (c,d) $U(x, y)$ normalized by local U_R and y_R: (a,c) FPG case and (b,d) suction-blowing case. △ represents the roughness crest elevation.

(defined as $\langle\widetilde{u}_i\widetilde{u}_i\rangle/2$) in the attached-flow regions are plotted in Figure 7(a,c), normalized by U_R, for the two cases respectively. Here y is normalized by $k_t \approx y_R$. The WKE is strong in the region around $y/k_t < 1$ only, consistent with the definition of RSL based on locally significant dispersive stress. The WKE is shown to scales largely on U_R^2, regardless of the pressure gradients. In the FPG case (Figure 7(a)), the slight difference among the profiles may be attributed to the change in roughness regimes as k_t^+ increases, reaching a nominally rough regime at $x/\theta_o \approx 450$, after which a better collapse is seen. As the rate of strain of $\widetilde{u}_i$ plays an important role in producing turbulence in rough-wall flows (Yuan & Piomelli 2014*c*), particularly for the non-equilibrium ones (Mangavelli *et al.* 2021), the result suggests some level of self-similarity in the turbulence production process despite the non-equilibrium pressure gradients. The dispersive shear stress (Figure 7(b,d)) in the RSL, on the other hand, does not scale on U_R^2. This suggests that the pressure gradients do have some effects on the dispersive stress anisotropy and subtle details of the $\widetilde{u}_i$ pattern inside the RSL.

3.4. *Weak-equilibrium Reynolds stresses inside RSL*

The streamwise development of the y-profiles of TKE, $\langle\overline{u_i'u_i'}\rangle/2$, and Reynolds shear stress magnitudes are analyzed for the suction-blowing case in Figure 8. Two sets of normalizations are used: (U_R^2, k_t) is used to focus on the development of the RSL region in

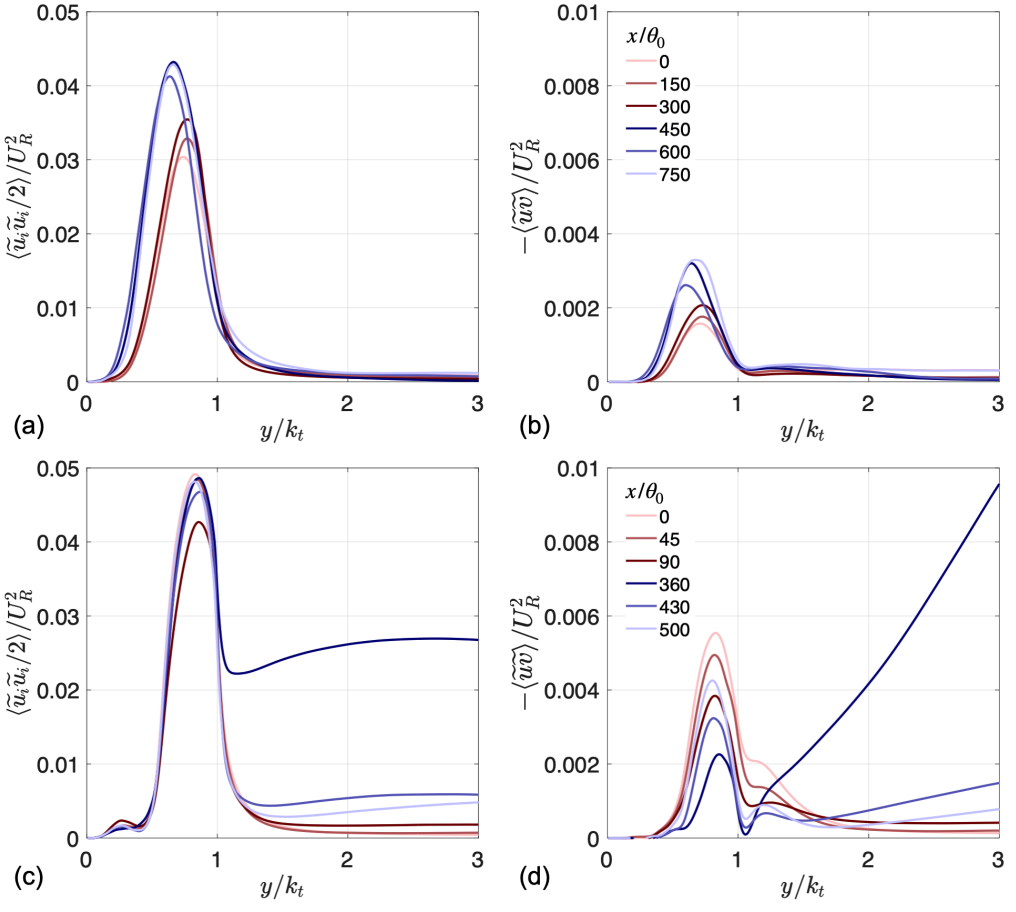

FIGURE 7. (a,c) WKE and (b,d) dispersive shear stress normalized by U_R^2: (a,b) FPG case and (c,d) suction-blowing case.

Figures 8(a,b), while (u_{hyb}^2, δ) is used to compare the outer layer profiles in Figures 8(c,d). The hybrid, friction-pressure-gradient velocity scale of Romero *et al.* (2022*b*) is defined as the velocity scale associated with the total shear stress, obtained by integrating the streamwise mean momentum equation once, assuming that the advection terms are negligible,

$$u_{hyb}(x,y)^2 = u_\tau(x)^2 + \frac{1}{\rho}\int_o^y \frac{\partial \langle \overline{P} \rangle (x,y)}{\partial x} dy. \tag{3.1}$$

Note that the pressure gradient integral in Equation 3.1 typically employs an additional assumption that the wall-normal pressure gradient is negligible (Romero *et al.* 2023, 2022*b*). However, here this term is calculated exactly since the flows are strongly non-equilibrium. u_{hyb} was found to be a better scaling than u_τ in smooth-wall APG flows for Reynolds stresses (Romero *et al.* 2022*b*) and turbulent velocity spectra (Romero *et al.* 2023). In rough-wall flows, the definition using Equation 3.1 applies to u_{hyb} calculation in the region outside the RSL only, as $u_\tau^2 = (1/\rho)\int_o^{y_R} f dy$ (where f is the body force due to the viscous and pressure drag of roughness) requires that the upper limit of the integral in Equation 3.1 to be higher than y_R. Therefore, only the outer region (i.e. region outside the RSL) is plotted for profiles normalized with u_{hyb} in Figures 8(c,d).

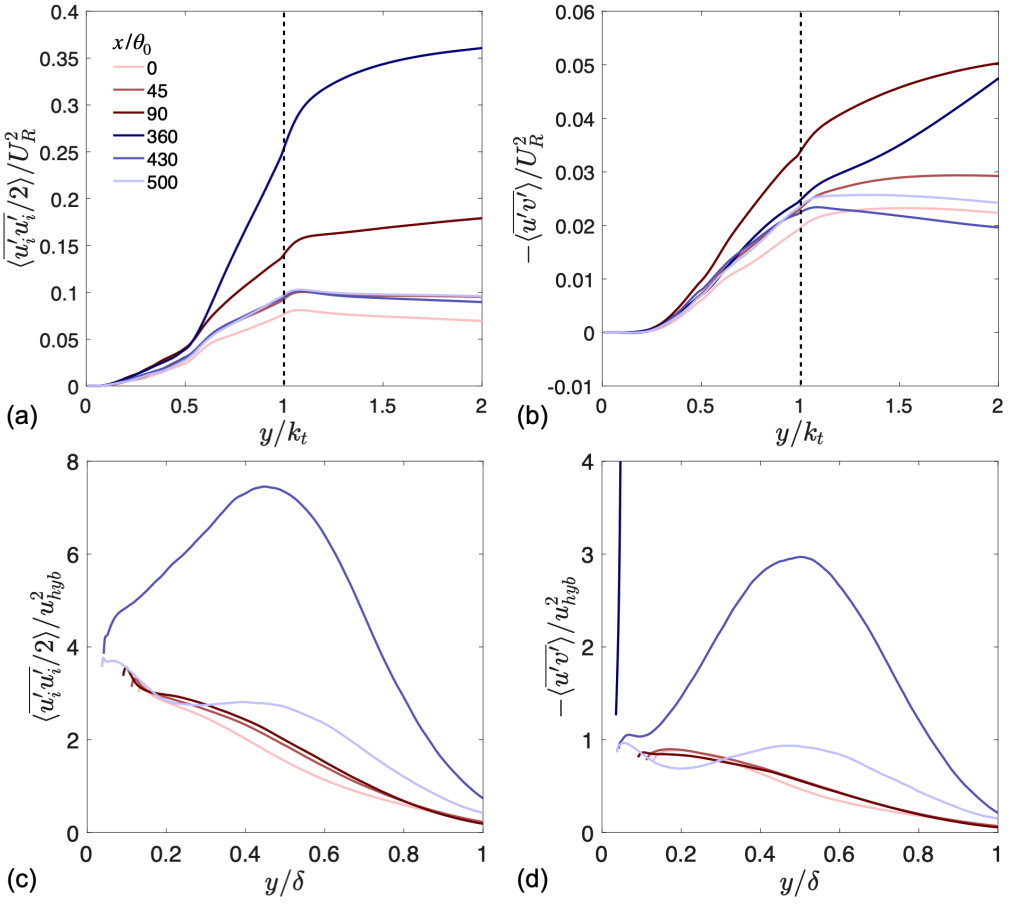

FIGURE 8. TKE (a,c) and Reynolds shear stress magnitude (b,d) in the suction-blowing case near the wall, normalized by U_R^2 (a,b) or u_{hyb}^2 (c,d). In (a,b), --- represents the roughness crest. In (c,d), only the region outside RSL (i.e. $y/k_t > 1$) is shown. (Note that, in (c) and (d), the $x/\theta_o = 360$ profile is fully or partially out of the picture due to extremely large values.)

Figure 8(a) show that the extent of the RSL coincides approximately with the near-wall peak of TKE, a phenomenon due to the intensification of TKE production at roughness crest as widely observed. In the non-equilibrium flow regions (i.e. at all x locations plotted except the first and the last ones), the TKE profiles inside the RSL are not collapsed by RSL scale, U_R^2. Instead, the TKE values in the outer layer display much less variation when normalized with u_{hyb} (Figure 8(c)) in the whole APG region before the separation point ($x/\theta_o = 0$, 45 and 90). In particular, the profiles almost fall on the same curve at the lower edge of the outer layer. After the reattachment ($x/\theta_o \geqslant 360$), u_{hyb}^2 does not scale outer-layer TKE, likely because of the history effect associated with the reattaching shear layer. Comparison between Figures 8(a) and (c) suggests that the RSL turbulence intensity does not scale with U_R, and that the reason is because of the pressure gradient effect on modifying the mean stress balance above the RSL.

For the Reynolds shear stress, when normalized by U_R^2, Figure 8(b) shows a better collapse in the RSL than that of TKE in Figure 8(a). A possible explanation is that the active motions producing turbulence are primarily associated with the wake-production inside the RSL, i.e. the conversion from the WKE to the TKE (Raupach & Shaw 1982).

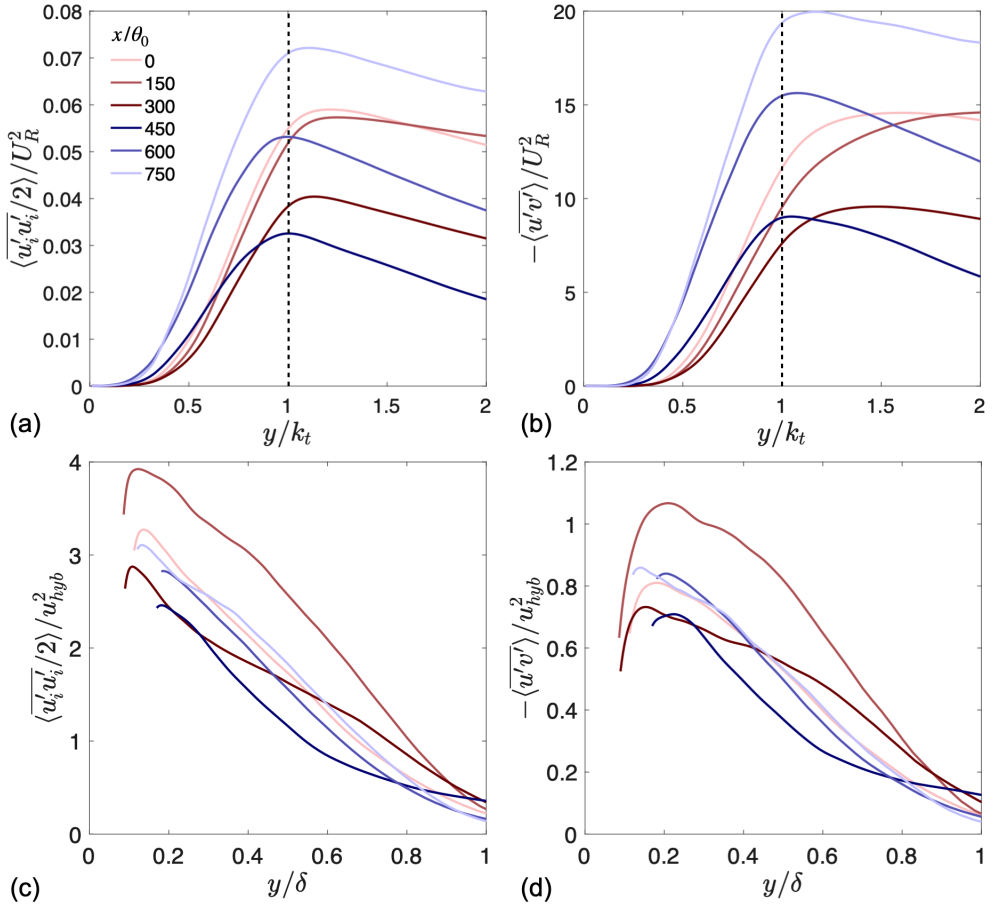

FIGURE 9. TKE (a,c) and Reynolds shear stress magnitude (b,d) in the FPG case near the wall, normalized by U_R^2 (a,b) or u_{hyb}^2 (c,d). In (a,b), **---** represents the roughness crest. In (c,d), only the region outside RSL (i.e. $y/k_t > 1$) is shown.

Given that the WKE scales well on U_R (Figure 7), the intensity of the active motions may scale well on U_R also. Outside the RSL the profiles differ, due to the lower $U_R(x)$ values near the separation bubble. When normalized by u_{hyb}, the Reynolds shear stress profiles in the outer layer again collapse overall very well, except for locations downstream of the reattachment.

For the FPG case, however, no RSL collapse is observed for either TKE or the Reynolds shear stress normalized by U_R^2 (Figures 9(a,b)). It is not clear what exactly the reason might be. The different Reynolds shear stress scaling in flows with opposite directions of pressure gradient may indicate some fundamental difference in how RSL turbulence reacts to strong pressure gradients of different signs or of different histories. Alternatively, it may be attributed to the change of roughness Reynolds number, as in the FPG case, the flow develops from a transitionally rough to the fully rough state. When normalized by u_{hyb}^2, a slightly smaller spread is seen for the TKE and the Reynolds shear stress (Figures 9(c,d)), particularly in peak values compared to U_R^2 normalization. However, the outer layer profiles are not very well collapsed under this normalization, perhaps due to the history effect and the non-negligible advection terms.

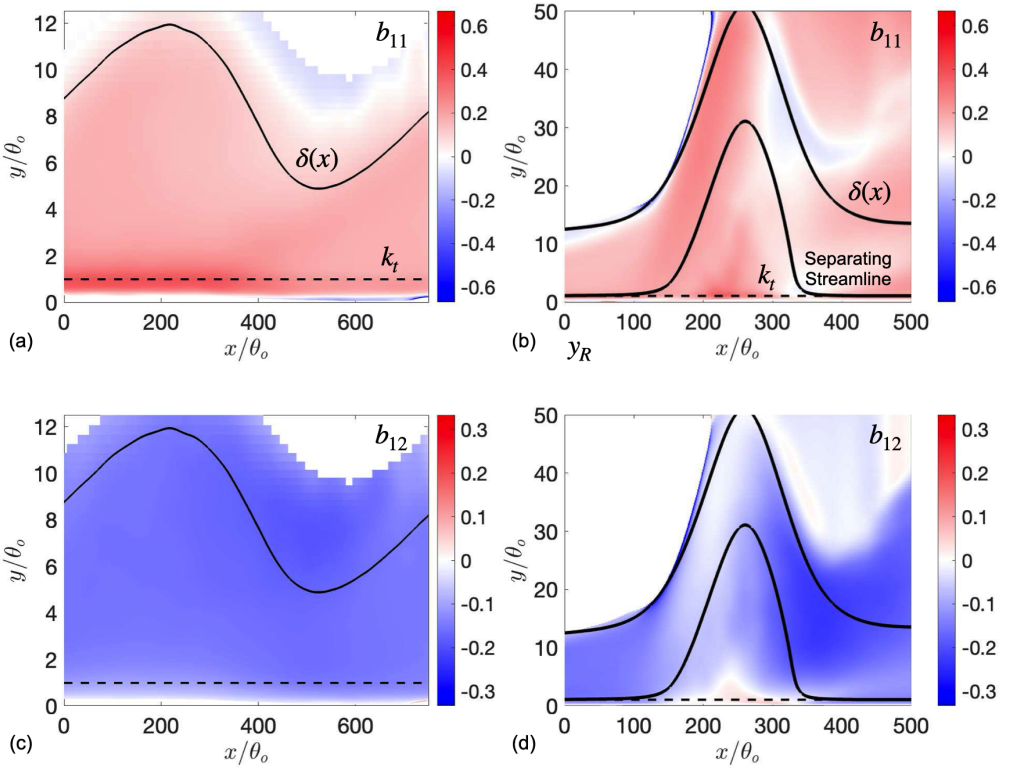

FIGURE 10. Reynolds stress anisotropy b_{11} (a,b) and b_{12} (c,d) in the FPG (a,c) and suction-blowing cases (b,d).

The results above show that turbulent fluctuations are not in general self-similar (i.e. equilibrium) inside the RSL. Next, the concept of "weak-equilibrium" condition (Girimaji 1996) is explored. Under this condition, the material derivative of the Reynolds stress anisotropy is negligible,

$$\frac{db_{ij}}{dt} = \frac{\partial b_{ij}}{\partial t} + U_k \frac{\partial b_{ij}}{\partial x_k} \approx 0, \tag{3.2}$$

where $b_{ij} = \langle \overline{u_i' u_j'} \rangle / \langle \overline{u_i' u_i'} \rangle - (1/3)\delta_{ij}$. In other words, the structure of the Reynolds stress tensor remains unchanged in time and space, following a fluid particle. It is a form of local equilibrium, rather than a bulk equilibrium with respect to far-field parameters such as freestream pressure gradients and integral lengths (Brereton 2025). In development of Reynolds stress models, the weak-equilibrium condition allows exact reduction of the differential transport equations into algebraic ones that are cheaper to solve (Rodi 1976; Girimaji 1996; Brereton 2024, 2025).

Figure 10 displays the contours of b_{11} and b_{12} in the two cases. Here, b_{ij} values are shown for the region with finite TKE (with values higher than 0.001 times of the maximum streamwise Reynolds stress values) only, to avoid singularities outside the boundary layer. As expected from wall-bounded shear flows, the Reynolds stress anisotropy is characterized by positive b_{11} values (ranging from approximately 0.2-0.4 throughout most of the boundary layers in the attached flow regions), indicating that a significant portion of the TKE is concentrated in the streamwise fluctuations, while b_{22} and b_{33} components (not shown) are negative, except in the vicinity of the reattachment point. For the FPG case in the outer layer ($y > k_t$), b_{11} increases slightly at $x/\theta_o \approx 400$, a

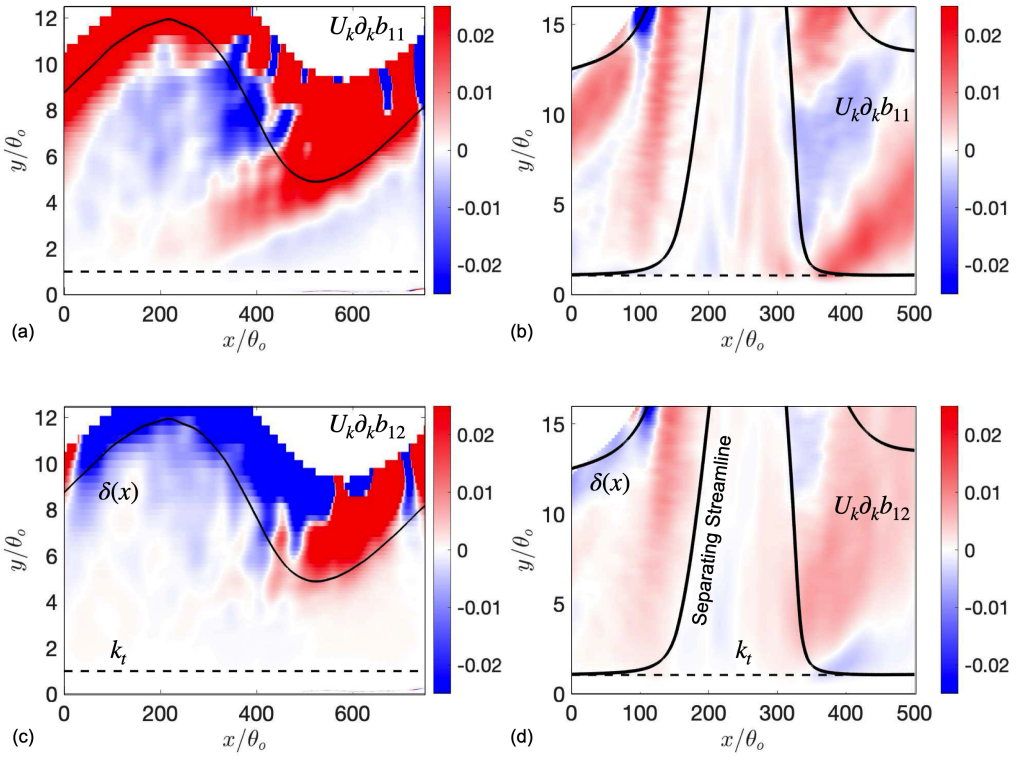

FIGURE 11. Material derivatives of b_{11} (a,b) and b_{12} (c,d) in the FPG (a,c) and suction-blowing cases (b,d). In (a,c), normalization is done with local mean shear ($\partial U/\partial y$), while in (b,d), the y-local mean shear at $x/\theta_o = 0$ is used to avoid singularity due to separation.

sign of rapid distortion under strong shear ($\partial U/\partial y$); inside the RSL ($y < k_t$), however, the turbulence becomes more isotropic as b_{11} decreases with the acceleration. b_{12}, however, stays almost invariant throughout the boundary layer, including the RSL. In the suction-blowing case, the Reynolds stress anisotropy mainly varies inside the detached shear layer and the boundary layer immediately downstream of the reattachment. Key features include a more anisotropic detached shear layer and more prominent Reynolds shear stress near reattachment. Inside the RSL, no significant changes of b_{ij} is observed except for the region inside the mean separation bubble.

The material derivatives of b_{11} and b_{12} are shown in Figure 11 for both cases. Here, $db_{ij}/dt = U_k \partial b_{ij}/\partial x_k$ due to the flow steadiness. db_{ij}/dt values are normalized using the time scale associated with the mean shear rate, $(\partial U/\partial y)^{-1}$. A high magnitude of dimensionless db_{ij}/dt will indicate a fast change of the structure of the Reynolds stress tensor with respect to the timescale of the mean strain rate, i.e. a departure from the weak equilibrium condition. For the FPG case, the local mean shear values are used. For the suction-blowing case, however, the y-distribution of mean shear at $x/\theta_o = 0$ is used for normalization, to eliminate singularities at the detachment and reattachment points where $\partial U/\partial y = 0$. The very large values outside the boundary layer should be ignored as they are artifacts caused by small mean shear magnitudes. In the outer layer of the FPG boundary layer (Figure 11(a,c)), a fast rate of change of b_{11} again demonstrates the rapid distortion under a stronger mean shear brought by the acceleration. In this region, the rate of change of b_{12} is weaker in comparison, though not entirely negligible. Similarly, in

the suction-blowing case the anisotropy components show non-zero rate of change inside the shear layer above $y = k_t$, attached or detached. In contrast, for both cases, b_{11} and b_{12} are negligible inside the RSL throughout the x domain. The b_{ij} variations inside the RSL, as shown in Figure 10, appear to be caused by the movement of fluid particles. The results indicate that, although the Reynolds stresses inside the RSL are not self-similar in a general sense under the normalization tested herein (Figures 8 and 9), the turbulence there appears to be in weak-equilibrium, with Reynolds stresses retaining self-similarity in time and space, when scaled by the TKE.

4. Conclusions

Two non-equilibrium spatially developing turbulent boundary layers over rough walls are compared, with the focus on the roughness-sublayer (RSL) statistics in attached flows. The data come from DNS and LES simulations of boundary layers, with either a strong favorable pressure gradient (FPG) or a suction-blowing boundary condition that leads to adverse pressure gradient (APG) then FPG inducing a separation bubble. Comparisons are made on how weak to strong non-equilibrium pressure gradients in both signs affect rough-wall boundary layer development and the RSL flow statistics. Results show that, regardless of the magnitude, direction and history of the mean streamwise pressure gradients, some flow properties in the RSL appear invariant when normalized using the RSL scales: (y_R, U_R), where y_R is the RSL thickness, measured from the trough elevation, and $U_R(x) = U(x, y_R)$ is the mean streamwise velocity at the edge of the sublayer. When normalized using this set of scales, the total drag, mean streamwise velocity profiles and wake kinetic energy profiles are shown to be invariant in x, while this is not the case when using u_τ or U_e instead of U_R. In addition, in the attached-flow regions, y_R is constant regardless of the pressure gradient.

In contrast, the RSL profiles of Reynolds stresses normalized by U_R^2 are not self-similar in general, although some level of self-similarity is observed for the Reynolds shear stress in the suction-blowing case. Given that the Reynolds stresses scale well on u_{hyb}^2 at the edge of the RSL, the lack of self-similarity inside the RSL is probably due to the effect of pressure gradient on modifying the mean stress balance in the outer layer. The RSL Reynolds stresses, however, appear to be in local equilibrium as the Reynolds stress anisotropy remains invariant in space, following a fluid particle.

These results provide insights into developing physics-based turbulence closures that do not resolve the roughness sublayer. The observed self-similarity in time-mean flow statistics indicates that the mean-flow pattern around the roughness elements inside the RSL is invariant, regardless of pressure gradient, as far as the roughness Reynolds number is sufficiently high. The same observation was made for RSL in transient channels (Mangavelli & Yuan 2023; Mangavelli *et al.* 2021). This observation is also consistent with the conjecture of Volino *et al.* (2024) that k_s/k does not change with pressure gradients (where k is a physical roughness height). The scaling of $\tau_w \sim U_R^2$ needs to be respected in WMLES and RANS models and can be used to evaluate the appropriateness of existing roughness treatments in these models. The weak-equilibrium condition of Reynolds stresses inside the RSL suggests that existing algebraic Reynolds stress models may be extendible to rough-wall flows.

From a physical point of view, future work needs to systematically test the self-similarity observed herein for flows with different pressure gradients, history, roughness types, and roughness Reynolds numbers. In addition, the k_s^+ threshold above which the self-similarity applies (as well as its possible dependence on pressure gradients) needs to be investigated.

Acknowledgments

This work was partially supported by the Office of Naval Research under grant N00014-17-1-2102 (Program Manager: Dr. Peter Chang). Computational resources were provided by the Institute for Cyber-Enabled Research at Michigan State University. JY gratefully acknowledges Prof. Wen Wu (University of Mississippi, Oxford, MS, USA) for his guidance on the initial setup of adverse-pressure-gradient boundary layer simulations.

REFERENCES

Aupoix, B. & Spalart, P. R. 2003 Extensions of the Spalart–Allmaras turbulence model to account for wall roughness. *Int. J. Heat Fluid Flow* **24**, 454–462.

Brereton, G. J. 2024 "Return to equilibrium" anisotropy model for non-equilibrium Reynolds stress closures. *Phys. Fluids* **36**, 035121.

Brereton, G. J. 2025 Further assessments of a "return to equilibrium" anisotropy model for non-equilibrium Reynolds stress closures. *Phys. Fluids* **37**, 015180.

Brereton, G. J., Aghaei Jouybari, M. & Yuan, J. 2021 Towards modeling of turbulent flow over surfaces of arbitrary roughness. *Phys. Fluids* **33**, 065121–1—13.

Chan, L., MacDonald, M., Chung, D., Hutchins, N. & Ooi, A. 2015 A systematic investigation of roughness height and wavelength in turbulent pipe flow in the transitionally rough regime. *J. Fluid Mech.* **771**, 743–777.

Dutta, R., Nicolle, J., Giroux, A.-M. & Piomelli, U. 2016 Evaluation of turbulence models on roughened turbine blades. In *IOP Conf. Series: Earth and Environmental Science*, , vol. 49, p. 062007.

Germano, M., Piomelli, U., Moin, P. & Cabot, W. H. 1991 A dynamic subgrid-scale eddy viscosity model. *Phys. Fluids A* **3**, 1760–1765.

Girimaji, S. S. 1996 Fully explicit and self-consistent algebraic Reynolds stress model. *Theor. Comput. Fluid Dyn.* **8**, 387–402.

Jackson, P. S. 1981 On the displacement height in the logarithmic velocity profile. *J. Fluid Mech.* **111**, 15–25.

Klewicki, J. C., Sandberg, R., Knopp, T., Devenport, W., Fritsch, D. J., Vishwanathan, V., Volino, R. J., Toxopeus, S., McKeon, B. J. & Eca, L. 2024 On the physical structure, modelling and computation-based prediction of two-dimensional, smooth-wall turbulent boundary layers subjected to streamwise pressure gradients. *J. Turbul.* **25**, 345–368.

Lund, T. S., Wu, X. & Squires, K. D. 1998 Generation of inflow data for spatially-developing boundary layer simulations. *J. Comput. Phys.* **140**, 233–258.

Mangavelli, S. C. & Yuan, J. 2023 Effects of form-induced velocity in rough-wall turbulent channel flows. *J. Turbul.* **24**, 14–35.

Mangavelli, S. C., Yuan, J. & Brereton, G. J. 2021 Effects of surface roughness topography in transient channel flows. *J. Turbul.* **22**, 434–460.

Orlanski, I. 1976 A simple boundary condition for unbounded hyperbolic flows. *J. Comput. Phys.* **21**, 251–269.

Piomelli, U. & Yuan, J. 2013 Numerical simulations of spatially developing, accelerating boundary layers. *Phys. Fluids* **25**, 101304–1—21.

Pokrajac, D., Campbell, L. J., Nikora, V. & Manes, C. adn McEwan, I. 2007 Quadrant analysis of persistent spatial velocity perturbations over square-bar roughness. *Exp. Fluids* **42**, 413–423.

Raupach, M. R. & Shaw, R. H. 1982 Averaging procedures for flow within vegetation canopies. *Bound.-Lay. Meteorol.* **22**, 79–90.

Rodi, W. 1976 A new algebraic relation for calculating the Reynolds stress. *Z Angew. Math. Mech.* **56**, T219.

Romero, S., Zimmerman, S., Philip, J. & Klewicki, J. C. 2023 Velocity spectra and scale decomposition of adverse pressure gradient turbulent boundary layers considering history effects. *Int. J. Heat Fluid Fl.* **102**, 109143.

Romero, S., Zimmerman, S., Philip, J., White, C. & Klewicki, J. C. 2022*a* Properties

of the inertial sublayer in adverse pressure-gradient turbulent boundary layers. *J. Fluid Mech.* **937**, A30.

Romero, S., Zimmerman, S. J., Philip, J. & Klewicki, J. C. 2022*b* Stress equation based scaling framework for adverse pressure gradient turbulent boundary layers. *Int. J. Heat Fluid Fl.* **93**, 108885.

Spalart, P.R. 1986 Numerical study of sink-flow boundary layers. *J. Fluid Mech.* **172**, 307–328.

Taylor, R. P., Coleman, H. W. & Hodge, B. K. 1985 Prediction of turbulent rough-wall skin friction using a discrete element approach. *J. Fluids Eng.* **107**, 251–257.

Vishwanathan, V., Fritsch, D. J., Lowe, K. T. & Devenport, W. J. 2023 History effects and wall-similarity of non-equilibrium turbulent boundary layers in varying pressure gradient over rough and smooth surfaces. *Int. J. Heat Fluid Fl.* **102**, 109145.

Volino, R. J., Devenport, W. J. & Piomelli, U. 2022 Questions on the effects of roughness and its analysis in non-equilibrium flows. AIAA Paper 2022-0695.

Volino, R. J., Fritsch, D. J., Devenport, W. J., Eca, L., Garcia-Mayoral, R., McKeon, B. J., Piomelli, U., Chung, D., Vishwanathan, V., Kerkvliet, M., Toxopeus, S. & Hutchins, N. 2024 Effects of roughness on non-equilibrium turbulent boundary layers. *J. Turbul.* **25**, 369–385.

Volino, R. J. & Schultz, M. P. 2023 Comparison of smooth- and rough-wall non-equilibrium boundary layers with favourable and adverse pressure gradients. *J. Fluid Mech.* **959**, A35–1—40.

Wilcox, D. C. 2006 *Turbulence modeling for CFD*. DCW Industries.

Wu, W. & Piomelli, U. 2018 Effects of surface roughness on a separating turbulent boundary layer. *J. Fluid Mech.* **841**, 552–580.

Yuan, J., Nicolle, J., Piomelli, U. & Giroux, A.-M. 2014 Modelling roughness and acceleration effects with application to the flow in a hydraulic turbine. *IOP Conf. Series: Earth and Environmental Science* **22**, 022016.

Yuan, J. & Piomelli, U. 2014*a* Estimation and prediction of the roughness function on realistic surfaces. *J. Turbul.* **15**, 350–365.

Yuan, J. & Piomelli, U. 2014*b* Numerical simulations of sink-flow boundary layers over rough surfaces. *Phys. Fluids* **26**, 015113–1—015113–28.

Yuan, J. & Piomelli, U. 2014*c* Roughness effects on the Reynolds stress budgets in near-wall turbulence. *J. Fluid Mech.* **760**, R1.

Yuan, J. & Piomelli, U. 2015 Numerical simulation of a spatially developing accelerating boundary layer over roughness. *J. Fluid Mech.* **780**, 192–214.